

Elasto-Raman scattering: Arsenic optical phonon as a probe of nematicity in BaFe₂As₂Jean-Côme Philippe^{1,*}, Jimmy Faria,¹ Anne Forget,² Dorothée Colson,² Sarah Houver,¹ Maximilien Cazayous,¹ Alain Sacuto,¹ and Yann Gallais^{1,†}¹*Université de Paris, Matériaux et Phénomènes Quantiques, CNRS, 75013 Paris, France*²*Service de Physique de l'Etat Condensé, DSM/DRECAM/SPEC, CEA Saclay, Gif-sur-Yvette, 91191, France*

(Received 12 October 2021; revised 30 December 2021; accepted 5 January 2022; published 24 January 2022)

We report a Raman scattering study of nematic degrees of freedom in the iron-based superconductor parent compound BaFe₂As₂ under tunable uniaxial strain. We demonstrate that the polarization resolved arsenic (As) phonon intensity can be used to monitor the nematic order parameter as a function of both temperature and strain. At low temperature in the nematic ordered phase, we use it to track the continuous and reversible orientation of nematic domains under variable strain. At higher temperatures, the evolution of the As phonon intensity under strain reflects an enhanced nematic susceptibility close to the nematic transition T_S . Its temperature dependence under strong strain qualitatively follows the expected behavior of an Ising order parameter under a symmetry-breaking field. Our elasto-Raman study illustrates the interest of combining selective anisotropic strain with a symmetry-resolved probe like Raman scattering. Elasto-Raman scattering can be applied to a wide variety of quantum materials where uniaxial strain tunes electronic orders.

DOI: [10.1103/PhysRevB.105.024518](https://doi.org/10.1103/PhysRevB.105.024518)**I. INTRODUCTION**

Anisotropic strain is emerging as a valuable nonthermal tuning parameter of quantum materials [1–4]. In the case of iron-based superconductors (Fe SCs) where a nematic phase breaking the C_4 rotational symmetry of the underlying lattice is found in close proximity of superconductivity [5], uniaxial strain acts as a conjugate field of the nematic order parameter. It is therefore a useful tool to study nematic susceptibilities like elastoresistivity [1,6,7], the change in resistivity anisotropy under uniaxial strain, but also more generally to study the interplay between nematic and superconducting orders [8]. Moreover, applying a uniaxial strain whose symmetry is transverse to the one of the nematic order parameter can provide an alternative path to tune a material toward a nematic quantum critical point with enhanced quantum critical fluctuations [9,10].

Initially limited to transport measurements [1–3,11–13], techniques under tunable uniaxial strain have been recently implemented and leveraged to study several superconducting materials, with, in the case of Fe SCs, a particular focus on accessing nematic degrees of freedom [14–23]. However, few of these techniques are symmetry resolved and as such they do not directly access the nematic order parameter. For example, they cannot easily distinguish nematic order from the simultaneous stripelike magnetic order found in many Fe SCs. Because it is symmetry selective thanks to specific selection rules, Raman scattering has been shown to provide important insights into nematic degrees of freedom in Fe SCs in both their normal and superconducting states even under nominally zero strain [24–28]. However, combining tunable anisotropic strain with symmetry-resolved Raman scattering

has so far been limited to measurements under fixed uniaxial stress, aimed mostly at obtaining detwinned crystals [29,30]. Extending Raman measurements in Fe SCs in a tunable uniaxial strain environment therefore appears desirable.

Here, using a low-temperature Raman scattering setup under continuously variable uniaxial strain, hereafter called elasto-Raman scattering, we study the effect of uniaxial strain on nematic order by looking at Raman-active optical phonons. We focus on BaFe₂As₂, a prototypical Fe SC showing nematic order. We show that the As optical phonon can serve as a sensitive probe of the nematic order parameter under varying strain. First, using the anisotropy of the As phonon Raman tensor, we demonstrate the monitoring of strain-induced orientation of nematic domains at low temperature. Second, above the orthorhombic-nematic transition temperature T_S , we show that the As phonon intensity can be used to track the strain-induced nematic order parameter, and demonstrate that it is a sensitive probe of the underlying electronic nematic susceptibility. Finally, we show that the nematic order parameter under strong strain follows the behavior expected for an Ising order parameter under symmetry breaking. This indicates that the As phonon Raman intensity is mostly sensitive to nematic order as opposed to the stripelike magnetic order. Complications in the quantitative interpretation of the data close to T_S , arising from the temperature and strain dependence of the elastic constants, are also discussed. Our paper establishes elasto-Raman scattering as a promising tool for anisotropic strain-control studies of the complex phase diagrams found in many quantum materials.

II. PIEZO-BASED ELASTO-RAMAN SCATTERING SETUP

Dating back to the seminal work on electric field and anisotropic stress effects on Raman scattering phonons in semiconductors and insulators, there is a relatively long his-

*jeancome.philippe@u-paris.fr

†yann.gallais@u-paris.fr

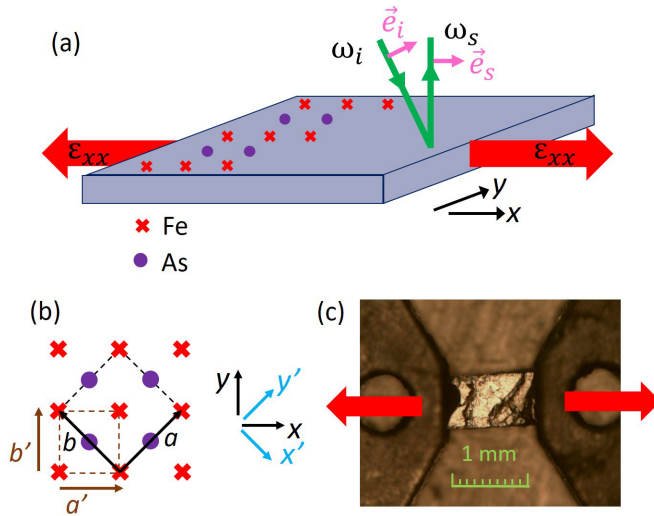


FIG. 1. (a) Sketch of the sample and strain configuration. The green arrows denote the incident and scattered light propagation directions, the pink arrows the polarization directions. (b) Definition of the crystallographic axes a , b (two-Fe tetragonal unit cell) and a' , b' (one-Fe unit cell) with respect to the laboratory frames (xy) and ($x'y'$) (the latter being rotated by 45° with respect to xy). (c) Top view picture of the mounted sample. In (a) and (c), the red arrows denote the directions of the applied stress and the ϵ_{xx} strain.

tory of morphic effects, i.e., the reduction of the crystal symmetry by an applied force, in crystals [31–36]. Early Raman studies under stress, and some recent ones on Fe SCs [29,30], have been performed under constant uniaxial stress with limited tunability and control over the actual strain applied. Our experimental setup is based on a uniaxial piezoelectric cell (CS130 from Razorbill Instruments) capable of applying *in situ* both tensile and compressive strains along a given direction [12]. The BaFe_2As_2 single crystal (Ba122) (dimensions 1.6 mm \times 700 μm \times 80 μm) is anchored at both ends using Loctite Stycast 2850FT epoxy (used with catalyst 24LV), each end being sandwiched in between two mounting plates. The strain cell is equipped with a capacitor-based sensor which can monitor *in situ* the change δL in the gap between the two moving sample plates, giving access to the nominal strain applied to the crystal along the x direction which we define as $\epsilon_{xx}^{\text{nom}} = \frac{\delta L}{L_0}$, where L_0 is the strain-free suspended sample length across the gap in the x direction (Fig. 1). The maximum amplitude variation of the gap is 10 μm at 4 K, corresponding to a maximum nominal strain of $\epsilon_{xx}^{\text{nom}} \sim 10^{-2}$ for the present crystal. The configuration of the piezostacks is such that their thermal contraction is compensated, thus minimizing the effect of temperature on the applied strain. Complications may arise from the differential thermal contraction between the titanium (Ti) body of the cell and the sample. For Ba122, however, this effect is minimal given the very similar temperature dependence of the expansion coefficient of Ti and Ba122 [37].

The uniaxial strain cell was mounted on a specially design copper mount inside the vacuum of a close-cycled optical cryostat. To compensate the relatively low thermal conductivity of Ti, copper braids were used to thermally anchor the cell with the second stage of the cryocooler. The temperature

was monitored using a silicon diode affixed directly on the cell body, next to the sample. Sample temperatures as low as 6.5 K could be reached. The piezostack voltages were controlled *in situ* via a dual 200 V power supply, and the capacitance of the displacement sensor was monitored using a Keysight LCR meter (model E4980AL). The Raman scattering geometry was noncollinear, with the incoming photon wave vector arriving at 45° with respect to the normal of the sample surface plane, and the outgoing photon wave vector lying along along the normal [Fig. 1(a)]. A single longitudinal mode solid-state laser emitting at 532 nm was used for the excitation. The laser spot size is estimated to be less than 50 μm , so we expect strain inhomogeneity to have less impact in our Raman measurements than in transport measurements performed in similar cells [2,3,8,10,37]. The outgoing photons were collected using a X20 long working distance microscope objective (NA=0.28) and analyzed via a triple grating spectrometer equipped with a nitrogen cooled CCD camera. A laser power of 10 mW was used for all spectra. Based on previous Raman measurements on Ba122, the laser heating was estimated to be about 1 K/mW [27,38]. The temperatures indicated in the following were corrected for this heating.

III. SAMPLE AND STRAIN CONFIGURATION

The Ba122 single crystal was cut along the crystallographic [110] direction (along the Fe–Fe bonds) using a wire saw. Transport measurements on single crystals from the same batch indicate an orthorhombic-nematic transition (quasicommitant with a spin-density-wave (SDW) transition) at $T_S = 138$ K. We define the direction of the applied strain ϵ_{xx} using the xyz laboratory frame. In the two-Fe unit cell of the FeAs plane, the tetragonal axes a and b are along the Fe–As bonds [Fig. 1(b)]. The strain ϵ_{xx} is applied at 45° of the tetragonal axes and is therefore parallel to the directions of axes a' and b' of the oneFe cell of the FeAs plane [Fig. 1(b)]. ϵ_{xx} directly couples to the nematic order parameter ϕ_{nem} of Ba122 which belongs to the B_{2g} representation in the two-Fe cell notation (B_{1g} in the one-Fe unit cell notation).

Despite working at constant strain ϵ_{xx} and under uniaxial stress conditions, we emphasize that, contrary to the stress, the actual strain applied is triaxial. This is due to the finite Poisson ratio linking the strain along the applied direction ϵ_{xx} and the one along the orthogonal directions ϵ_{yy} and ϵ_{zz} . The in-plane Poisson ratio is given by $\nu = -\frac{\epsilon_{yy}}{\epsilon_{xx}}$. An applied strain ϵ_{xx} along the [110] direction has both a nematic component B_{2g} and an in-plane isotropic component A_{1g} : $\epsilon_{xx} = \epsilon_{A_{1g}} + \epsilon_{B_{2g}}$. The relationship between the applied strain and the B_{2g} strain is given by $\epsilon_{B_{2g}} = \frac{1}{2}(1 + \nu)\epsilon_{xx}$. A further complication is the strain transmission to the sample which is in general not perfect as a result of the strain within the epoxy glue [12,13,37]. As a consequence, the actual strain experienced by the sample ϵ_{xx} will be, in general, different than the one measured by the capacitive sensor $\epsilon_{xx}^{\text{nom}}$ (see Appendix B for a discussion of these effects): $\epsilon_{xx} = \mu\epsilon_{xx}^{\text{nom}}$, where μ is the transmission ratio. Throughout the paper, the data will be shown as a function of $\epsilon_{xx}^{\text{nom}}$, but the effects of both strain transmission ratio μ and Poisson coefficient ν are important and will be discussed when interpreting the data. Note, however, that because of

the similar thermal contraction between Ti and Ba122, at $\epsilon_{xx}^{\text{nom}} = 0$ we also have $\epsilon_{xx} = \epsilon_{B_{2g}} = 0$.

IV. ARSENIC OPTICAL PHONON AND RAMAN SELECTION RULES

In this paper, we focus on the behavior of the Raman active optical phonon which involves the c -axis motion of the As atoms. The impact of strain on the electronic continuum will be discussed elsewhere. In Fe SCs, the strong sensitivity of the electronic properties to the As height in the unit cell is well-documented [39–42]. This link can be probed via the behavior of the Raman active As optical phonon, which modulates the As height. Indeed, previous Raman studies on several Fe SC materials have shown a significant impact of the nematic/SDW order on the As phonon line shape and intensity [30,38,43,44]. Here we will mainly be interested in the Raman selection rules of this phonon as a marker of the nematic order parameter. This will illustrate the interest of combining Raman selection rules with a tunable selective symmetry-breaking field like anisotropic strain.

Before proceeding with the results, we first briefly review the Raman selection rules for the As phonon in the tetragonal and orthorhombic/nematic phases. In the tetragonal phase, the As phonon belongs to the A_{1g} representation of the D_{4h} point group with the corresponding Raman tensor (written in the tetragonal two-Fe unit cell basis),

$$\Gamma_{\text{As}}^T = \begin{pmatrix} \alpha_{aa}^T & 0 & 0 \\ 0 & \alpha_{aa}^T & 0 \\ 0 & 0 & \alpha_{cc} \end{pmatrix}, \quad (1)$$

where the first two diagonal components are identical because of the C_4 symmetry of the tetragonal lattice. The components of the Raman tensor are given by the derivative of the dielectric tensor components $\hat{\epsilon}_{ij}$ (here we use the hat symbol to distinguish it from the strain) at the incoming photon frequency ω_L with respect to the phonon coordinates: $\alpha_{ij}^T = \frac{\partial \hat{\epsilon}_{ij}(\omega_L)}{\partial Q_{\text{As}}}$. Physically, the As atomic motion modulates the electronic band structure and thus the dielectric constant at the incoming photon energy (~ 2.4 eV). This electronic-mediated process makes Raman phonon intensities an indirect but very sensitive probe of the underlying electronic structure as in the case of As motion for Ba122 [30,44]. The Raman intensity for a given set of incoming (\mathbf{e}_i) and outgoing (\mathbf{e}_s) photon polarization vectors is proportional to the square of the tensor contracted by the photon polarization vectors:

$$I_{\text{As}}^{e_i e_s} = |\mathbf{e}_i^* \Gamma_{\text{As}} \mathbf{e}_s|^2. \quad (2)$$

For \mathbf{e}_i and \mathbf{e}_s parallel along any crystallographic direction, we have $I_{\text{As}}^{\parallel} = |\alpha_{aa}^T|^2$, while for perpendicular polarizations $I_{\text{As}}^{\perp} = 0$.

In the nematic phase, the As phonon belongs to the A_g representation of the D_{2h} point group. In this phase, we use the usual orthorhombic axes along the Fe–Fe bonds a' and b' which are rotated by 45° with respect to the tetragonal axes [Fig. 1(b)]. These two directions are now inequivalent and the Raman tensor reads in the $a'b'$ coordinates (henceforth, we will adopt the convention $a' < b'$ for the in-plane orthorhombic axes),

$$\Gamma_{\text{As}}^O = \begin{pmatrix} \alpha_{a'a'}^O & 0 & 0 \\ 0 & \alpha_{b'b'}^O & 0 \\ 0 & 0 & \alpha_{cc} \end{pmatrix}, \quad (3)$$

where the in-plane diagonal components are now distinct because of C_4 symmetry breaking. Below T_S , the intensity for parallel polarization is no longer isotropic when using parallel in-plane polarizations and we have $I_{\text{As}}^{a'a'} - I_{\text{As}}^{b'b'} = |\alpha_{a'a'}^O|^2 - |\alpha_{b'b'}^O|^2 \neq 0$. Previous Raman studies of Ba122 have shown that the difference between $\alpha_{a'a'}^O$ and $\alpha_{b'b'}^O$ is extremely large below T_S [30,38,43]. *Ab initio* calculations indicate that electronic or magnetic anisotropy rather than the lattice distortion itself is responsible for the large difference in the Raman tensor components [30]. The Raman tensor components can thus serve as local proxies of the electronic nematic order parameter as seen via the As atom displacement $\phi_{\text{nem}}^{\text{As}}$, defined as

$$\phi_{\text{nem}}^{\text{As}} = \frac{\alpha_{a'a'}^O - \alpha_{b'b'}^O}{\alpha_{a'a'}^O + \alpha_{b'b'}^O}, \quad (4)$$

which has the same B_{2g} symmetry as the electronic nematic order parameter. This quantity can be accessed from the measured Raman spectra in two different polarization configurations with incoming and outgoing photons, respectively, parallel to a' and b' orthorhombic axes,

$$I_{\text{As}}^{a'a'} - I_{\text{As}}^{b'b'} = \eta^2 \phi_{\text{nem}}^{\text{As}}, \quad (5)$$

where $\eta = \alpha_{a'a'}^O + \alpha_{b'b'}^O$. We note that $I_{\text{As}}^{a'a'} - I_{\text{As}}^{b'b'}$ will be sensitive to domain formation and will reflect the nematic order parameter $\phi_{\text{nem}}^{\text{As}}$ only in the presence of a single nematic domain under the laser spot.

An alternative marker of the nematic order parameter is the activation of the As phonon intensity in crossed polarizations along the tetragonal axes a and b : $I_{\text{As}}^{ab} = |\alpha_{a'a'}^O - \alpha_{b'b'}^O|^2 \neq 0$. I_{As}^{ab} transforms like the square of the nematic order parameter: $|\alpha_{a'a'}^O - \alpha_{b'b'}^O|^2 \sim (\phi_{\text{nem}}^{\text{As}})^2$. Contrary to the previous quantity, I_{As}^{ab} is insensitive to domain formation and directly reflects $(\phi_{\text{nem}}^{\text{As}})^2$:

$$I_{\text{As}}^{ab} = \eta^2 (\phi_{\text{nem}}^{\text{As}})^2. \quad (6)$$

In this paper, we will use $I_{\text{As}}^{a'a'} - I_{\text{As}}^{b'b'}$ to assess nematic domain population and I_{As}^{ab} as a local marker of the nematic order parameter. Note that the directions of the orthorhombic axes a' and b' will, in general, be spatially dependent below T_S due to domain formation. They will also depend on the applied strain. To avoid ambiguities, we will therefore label the direction of photon polarizations using the laboratory frames xyz and $x'y'z$ rather than using crystallographic axes.

V. ORIENTATION OF NEMATIC TWIN DOMAINS BELOW T_S

We first discuss the monitoring of nematic twin-domain orientations under strain. For this, we use the As phonon polarization-resolved intensity at 17 K, deep in the nematic-orthorhombic phase. Figure 2(a) displays As phonon Raman spectra for different values of $\epsilon_{xx}^{\text{nom}}$ and for parallel polarizations along (xx) and perpendicular (yy) to the applied strain.

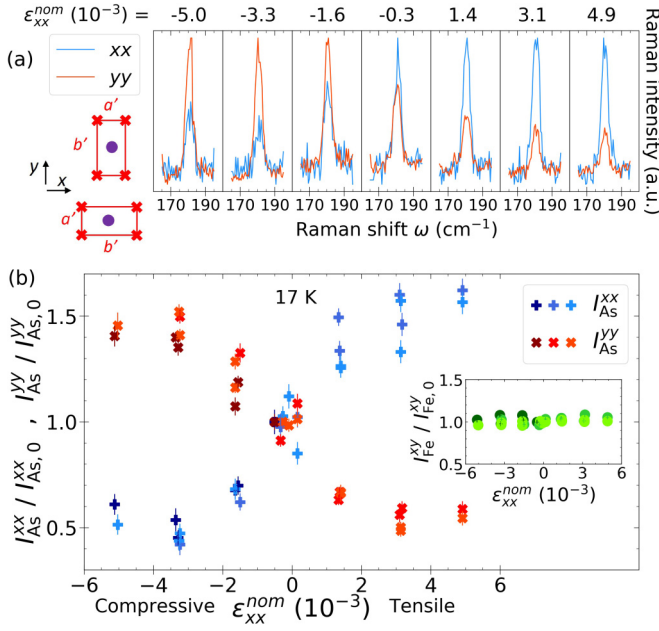


FIG. 2. Orientation of nematic twin domains at 17 K. (a) As phonon Raman spectra in the xx and yy polarization configurations for different strains. Here, the notations used for the polarization configurations indicate the direction of the incoming photon polarization followed by the direction of the outgoing photon polarization. The bottom left sketch depicts orientations of the two domains in the xy laboratory frame. (b) Dependence of the As phonon intensities in xx and yy polarization configurations with respect to strain. Inset: Dependence of the Fe phonon intensity in the B_{1g} xy polarization configuration with strain. We evaluated $I_{As,0}^{xx}$ as the mean of I_{As}^{xx} data points for the strains close to $\epsilon_{xx}^{nom} = 0$ (and likewise for $I_{As,0}^{yy}$ and $I_{Fe,0}^{xy}$). To assess the robustness of the obtained trends, for each of the three plotted quantities (I_{As}^{xx} , I_{As}^{yy} , I_{Fe}^{xy}), we plot three different sets of data obtained successively on the same sample, with three different shades of blue, red, and green, respectively, for I_{As}^{xx} , I_{As}^{yy} and I_{Fe}^{xy} .

The respective intensities I_{As}^{xx} and I_{As}^{yy} are strongly sensitive to the applied strain: For compressive strains $\epsilon_{xx}^{nom} < 0$, we have $I_{As}^{xx} < I_{As}^{yy}$ but for tensile strain $I_{As}^{xx} > I_{As}^{yy}$. We define $I_{As,0}^{xx} = I_{As}^{xx}(\epsilon_{B_{2g}} = 0)$ and, respectively, for $I_{As,0}^{yy}$. The crossover is continuous with one polarization configuration gaining intensity at the expense of the other upon varying strain. By contrast, the intensity of the B_{1g} Fe optical phonon mode hardly changes with strain [see inset of Fig. 2(b)].

A quantitative evaluation of the As phonon intensities I_{As}^{xx} and I_{As}^{yy} as a function of strain can be obtained by fitting it with a Gaussian line shape. The result is shown in Fig. 2(b) for three different cycles of compression and tension. The overall behavior is symmetric with respect to both strain and polarization directions and can be understood by a gradual modification of the population of nematic twin domains under compression/tensile strain with the presence of two different types of domains, with the shorter axis a' being along the laboratory frame direction x or y [Fig. 2(a)]. Calling $\beta(\epsilon_{xx}^{nom})$ the fraction of domains with the shorter axis a' aligned along the direction of applied stress x , we have

$$I_{As}^{xx} = \beta |\alpha_{a'a'}^0|^2 + (1 - \beta) |\alpha_{b'b'}^0|^2 \quad (7)$$

and, equivalently,

$$I_{As}^{yy} = \beta |\alpha_{b'b'}^0|^2 + (1 - \beta) |\alpha_{a'a'}^0|^2. \quad (8)$$

At zero strain, the nematic domains are equiprobable, giving $\beta(\epsilon_{xx}^{nom} = 0) = 0.5$ and therefore the phonon intensity is independent of the photon polarization $I_{As,0}^{xx} = I_{As,0}^{yy} = \frac{1}{2}(|\alpha_{a'a'}^0|^2 + |\alpha_{b'b'}^0|^2)$ as observed experimentally. Under large strain, the area under the laser spot becomes essentially single domain: The shorter orthorhombic axis a' is parallel (perpendicular) to the x direction for compression (tension). This results in $\beta = 1$ (compression) or $\beta = 0$ (tension). This yields $I_{As}^{xx} \propto |\alpha_{a'a'}^0|^2$ and $I_{As}^{yy} \propto |\alpha_{b'b'}^0|^2$ for strong compression and $I_{As}^{xx} \propto |\alpha_{b'b'}^0|^2$ and $I_{As}^{yy} \propto |\alpha_{a'a'}^0|^2$ for strong tension. Our data show that the modulus of the As Raman tensor element is larger along the longer orthorhombic axis: $|\alpha_{b'b'}^0|^2 \sim 3|\alpha_{a'a'}^0|^2$ in agreement with the Raman data under fixed compressive stress of Baum *et al.* [30]. The overall evolution of the intensity can be rationalized by noting that we expect the domain fraction β to follow a linear dependence as a function of strain: $\beta = \frac{1}{2}(1 - \frac{\epsilon_{B_{2g}}}{\epsilon_s})$, where $\epsilon_s = \frac{a' - b'}{a' + b'}$ is the local orthorhombic strain within each domain. This gives a linear dependence of the phonon intensity with applied strain:

$$I_{As}^{xx} = I_{As,0}^{xx} + \frac{\epsilon_{B_{2g}}}{2\epsilon_s} \eta^2 \phi_{nem}^{As}. \quad (9)$$

The above relation is valid only for $\epsilon_{B_{2g}} < \epsilon_s$ in the twinned domain regime. In this regime, the macroscopic strain of the crystal induced by the applied strain mostly occurs via domain-wall motion with no changes in the lattice constants a' and b' nor in the nematic order parameter (i.e., ϕ_{nem}^{As} is constant). In this regime, the energy barrier for domain formation is probably low [13], and indeed no significant hysteresis is observed in our data. We therefore expect the applied strain to be fully transmitted and entirely of B_{2g} symmetry: $\epsilon_{xx}^{nom} \sim \epsilon_{xx} \sim \epsilon_{B_{2g}}$. Upon applying further strain however, we enter a new regime where macroscopic strain can only occur via a change in the orthorhombic distortion itself and its associated nematic order parameter ϕ_{nem}^{As} .

The transition between the two regimes is apparent in our data of Fig. 2. For large compressive and tensile strains (above $\sim \mp 3 \times 10^{-3}$), the As phonon intensity becomes much more weakly dependent on the applied strain, indicating that the sample is close to being single domain. This value is close to the low-temperature orthorhombic distortion ϵ_s of Ba122 observed by x-ray diffraction measurements [45], confirming that the applied strain is fully transmitted to the crystal as a B_{2g} strain in the low strain regime. When $\epsilon_{xx}^{nom} > \epsilon_s$, β is fixed to 1 and 0 and the phonon intensity rather reflects the change of the nematic order parameter as probed by the local As Raman phonon tensor anisotropy ϕ_{nem}^{As} under applied strain, i.e., a form of local nematic susceptibility akin to the elastoresistivity measured by transport [1]. The nematic susceptibility is expected to be rather small deep in the nematic phase where ϕ_{nem}^{As} is fully saturated [1,24]. This likely explains the rather weak strain dependence of the phonon intensity above ϵ_s , which also supports our statement that the anisotropy in the Raman phonon intensity between the two polarizations comes mostly from the nematic electronic response, and is not due to

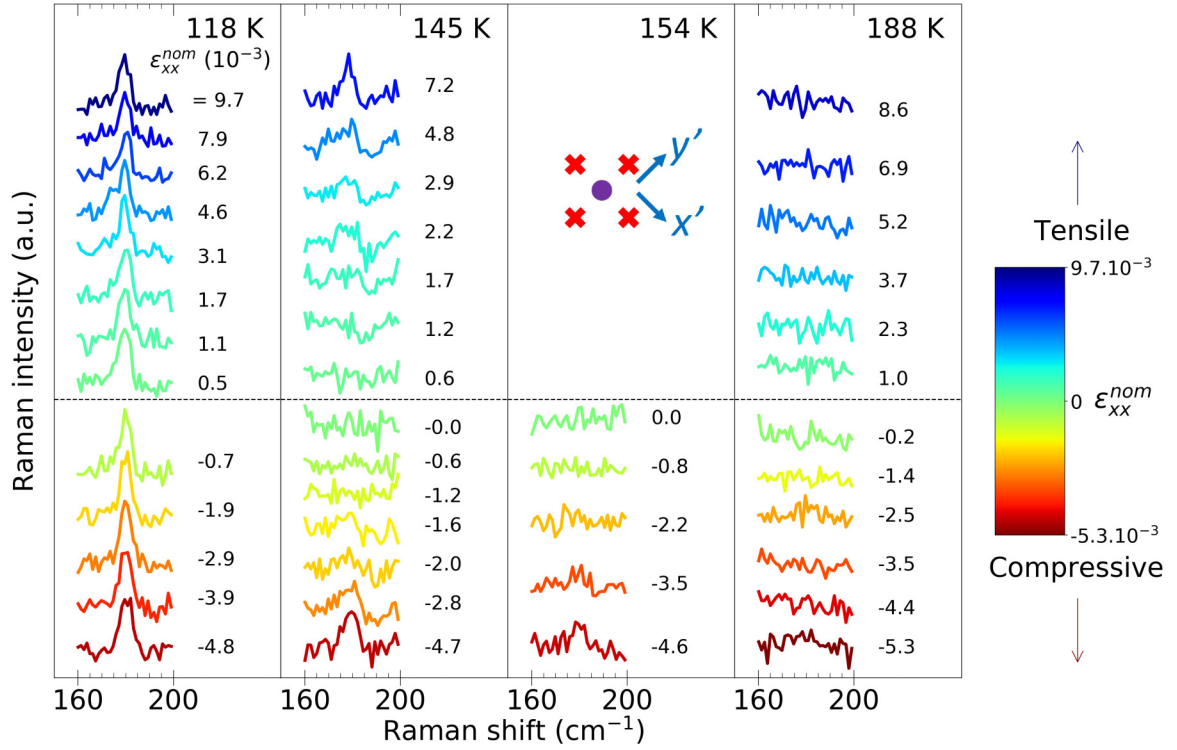


FIG. 3. Strain dependence of the As phonon Raman spectra in the $x'y'$ polarization configuration at four temperatures around T_S . Note that crystal likely broke during the last measurement at 118 K under strong tension $\epsilon_{xx}^{\text{nom}} = 9.7 \times 10^{-3}$. This precluded measurements at 154 K under tension: Only spectra under compression are shown.

the lattice distortion alone. We will discuss this effect in the next section when presenting the data close to T_S .

VI. STRAIN-TUNED NEMATICITY AROUND T_S

We now discuss the effect of strain on the As phonon close to the nematic transition temperature observed at $T_S = 138$ K under nominally zero strain. As phonon spectra at 118 K, 145 K, 154 K, and 188 K in the $x'y'$ configuration, where incident and outgoing polarizations are perpendicular and along the a and b tetragonal axes, are shown as a function of strain in Fig. 3. The spectra at $T = 145$ K $> T_S$ display the strongest strain dependence. At low strain, no phonon is detected in this geometry as dictated by tetragonal symmetry: $I_{\text{As}}^{x'y'} = |\alpha_{a'a'}^O - \alpha_{b'b'}^O|^2 = 0$. Upon applying both compressive and tensile strain, the phonon is activated in an approximate symmetric manner, indicating a strain-induced activation of the nematic order parameter $\phi_{\text{nem}}^{\text{As}}$ above T_S . Contrary to the spectra at 17 K discussed above, the activated phonon line shape is asymmetric with a rather pronounced Fano line shape that is evident at moderate strains, suggesting a significant coupling between the phonon and low-energy electronic excitations. The Fano line-shape asymmetry was also reported close, but below T_S in previous zero strain Raman data [38,43]. Increasing the temperature, we observe a significant weakening of the strain-induced activation of the As phonon. It is still visible at high strains at 154 K, but cannot be clearly resolved anymore within our signal-to-noise ratio at 188 K, except for $\epsilon_{xx} = -5.3 \times 10^{-3}$, where a weak and broad peak is detected. Note that the crystal broke during the measurements precluding measurements in tension at 154 K. Below T_S at 118 K, the

phonon is visible at all strains and only weakly depends on strain.

The evolution of the phonon intensity $I_{\text{As}}^{x'y'}$ as a function of strain and temperature was evaluated by fitting the phonon using a Fano line-shape analysis. $|\phi_{\text{nem}}^{\text{As}}| \propto (I_{\text{As}}^{x'y'})^{\frac{1}{2}}$ is shown in Fig. 4 for 118 K, 145 K, and 154 K (see Appendix A for details on the Fano line-shape fitting).

At 145 K, $|\phi_{\text{nem}}^{\text{As}}|$ shows a steep and strain-symmetric activation around $\epsilon_{xx}^{\text{nom}} = 0$. A much weaker effect is observed

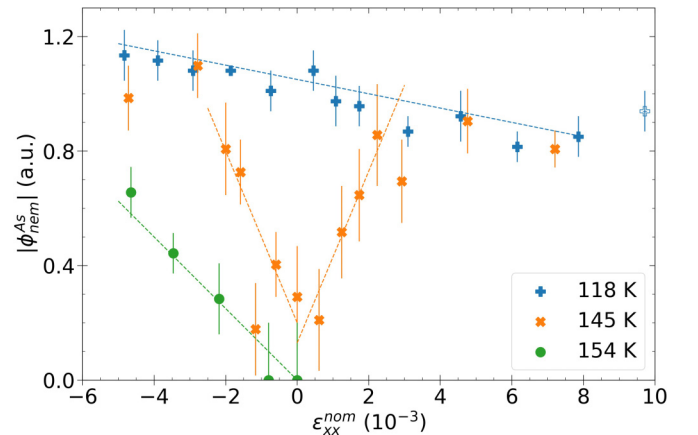


FIG. 4. Strain dependence of the As phonon derived nematic order parameter $|\phi_{\text{nem}}^{\text{As}}|$ at three temperatures around T_S . The dashed lines are guides to the eye and not fits of the data. The empty symbol at 118 K at high tensile strain indicates that we suspect that the sample broke at this point.

at 154 K with an initial slope $\frac{\partial |\phi_{\text{nem}}^{\text{As}}|}{\partial \epsilon_{xx}^{\text{nom}}} (\epsilon_{xx}^{\text{nom}} \rightarrow 0)$ at least two times smaller. The symmetric behavior observed at 145 K shows that the phonon intensity is mostly sensitive to the B_{2g} component of the applied strain, in qualitative agreement with a strong nematic susceptibility close to T_S . At 118 K, the intensity follows a much weaker strain-asymmetric dependence, indicating a dominant effect coming from the isotropic A_{1g} component of the applied strain. We assign this dependence to the monotonic decrease/increase of both T_S and T_N upon tensile/compressive A_{1g} strain observed in transport measurements under in-plane uniaxial stress [37]. We also note that the weak dependence of the Raman phonon intensity with strain at 118 K is a further indication of the electronic rather than structural origin of the measured order parameter $\phi_{\text{nem}}^{\text{As}}$. For strains above $\sim \pm 3 \times 10^{-3}$, the phonon intensity at 145 K shows signs of saturation and reaches values close to the intensity observed below T_S at 118 K.

At first sight and taking the initial slope $\frac{\partial |\phi_{\text{nem}}^{\text{As}}|}{\partial \epsilon_{xx}^{\text{nom}}} (\epsilon_{xx}^{\text{nom}} \rightarrow 0)$ as a marker of a nematic susceptibility χ_{nem} , the results can be qualitatively understood in terms of a strongly temperature dependent electronic nematic susceptibility. The behavior of χ_{nem} above T_S is well documented by previous elastoresistivity, shear-modulus and zero-strain electronic Raman scattering measurements which all detect a clear enhancement of χ_{nem} close to T_S in Ba122 [1,24,46], in qualitative agreement with the observed behavior at 145, 154 and 188 K. At 118 K $|\phi_{\text{nem}}^{\text{As}}|$ does not show a symmetric behavior with respect to $\epsilon_{xx}^{\text{nom}}$. Instead it displays a monotonic behavior, indicating a strongly reduced nematic susceptibility below T_S . Note that at 118 K the regime of domain orientation is likely very narrow, below $|\epsilon_{xx}^{\text{nom}}| = 2 \times 10^{-3}$ and therefore has a limited impact on the data presented in Fig. 4. Since transport measurements are plagued by domain formation below T_S , our data suggest that $|\phi_{\text{nem}}^{\text{As}}|$ is a potentially interesting alternative marker to track the nematic susceptibility and order parameter both above and below T_S .

There are, however several caveats which must be addressed before linking the observed behavior to an enhanced nematic susceptibility. Formally, a nematic susceptibility is defined as a derivative of a nematic observable with respect to a nematic field. In our case, we can define it using our definition of the nematic order parameter as probed by the As phonon $\phi_{\text{nem}}^{\text{As}}$ as

$$\chi_{\text{nem}}^{\text{As}} = \frac{\partial \phi_{\text{nem}}^{\text{As}}}{\partial \epsilon_{B_{2g}}} \quad (10)$$

The initial slope can be written in terms of the above-defined nematic susceptibility:

$$\frac{\partial |\phi_{\text{nem}}^{\text{As}}|}{\partial \epsilon_{B_{2g}}} = |\eta| \frac{\phi_{\text{nem}}^{\text{As}}}{|\phi_{\text{nem}}^{\text{As}}|} \chi_{\text{nem}}^{\text{As}} \quad (11)$$

The main complication when using Eq. (11) to access $\chi_{\text{nem}}^{\text{As}}$ from our data stems from converting the nominal strain measured $\epsilon_{xx}^{\text{nom}}$ into the actual B_{2g} strain $\epsilon_{B_{2g}}$ experienced by the sample. Indeed, we have

$$\epsilon_{B_{2g}} = \frac{1}{2}(1 + \nu)\mu\epsilon_{xx}^{\text{nom}}, \quad (12)$$

where μ is the transmission coefficient and ν the Poisson ratio. Since we are not interested in the absolute value of $\chi_{\text{nem}}^{\text{As}}$ but only in its strain and temperature dependence, in general, it suffices that these coefficients are weakly dependent on both strain and temperature. In materials away from a structural instability, this condition is satisfied, but this is clearly not the case near T_S for Ba122. First, the Poisson ratio ν is strongly temperature dependent near T_S : At T_S the shear modulus $C_{66} \propto \frac{1-\nu}{1+\nu}$ goes to zero but it stiffens significantly away from T_S [46]. As a consequence, the applied strain is expected to be entirely B_{2g} symmetric at T_S , but to quickly acquire a significant A_{1g} component away from T_S . Fortunately, in the low-strain limit this effect can be taken into account via available data of the temperature dependence of elastic constant in Ba122 [47]. A second nontrivial effect comes from the transmission coefficient μ . Because the Young modulus along the orthorhombic direction also softens to zero at T_S [48], we expect the strain to be fully transmitted at T_S , but not away from it when the lattice hardens. Finite element simulations using available data on elastic constants were conducted to estimate the temperature dependence of μ (see Appendix B). Overall, the combination of these two effects gives corrections of ~ 1.3 and ~ 2 at low strain between 145 K and 154 K, and 145 K and 188 K respectively. The data indicate at least a factor of 2 between the slopes at 145 K and 154 K (Fig. 4). Given the absence of any resolved As phonon at 188 K up to at least $\epsilon_{xx}^{\text{nom}} = 4 \times 10^{-3}$, we can give a lower bound estimate of at least a factor of 4 between the experimental slopes at 145 K and 188 K. Therefore, we conclude that while these corrections are significant and must be accounted for in any quantitative discussion of the slope, they cannot fully account for the observed temperature dependence of the slopes at low strain. This observation confirms that $|\phi_{\text{nem}}^{\text{As}}|$ and $\chi_{\text{nem}}^{\text{As}}$ are not simple proxies of the lattice orthorhombicity $\epsilon_{B_{2g}}$ and shear modulus C_{66} , respectively, but have a significant component related to the purely electronic nematic order parameter and susceptibility.

Beyond the small strain regime, the reasoning above cannot apply: because of the increase of the nematic order parameter, the shear modulus at high strain is expected to stiffen with respect to its low strain value. The effect is expected to be particularly strong near T_S where the softening of the shear modulus will be significantly reduced at high strain and will recover its value at high temperature, far above the structural instability (see Appendix C for a discussion of these nonlinear effects). Indeed recent elasto-x-ray scattering data in Co doped Ba122 indicate that both the transmission coefficient and the Poisson ratio become essentially temperature independent for nominal strains above $\pm 3 \cdot 10^{-3}$ [20]. In our case, the strain-induced reduction of the Poisson ratio and transmission coefficient at 145 K could partly explain the saturation of $|\phi_{\text{nem}}^{\text{As}}|$ for $|\epsilon_{xx}^{\text{nom}}| > 4 \times 10^{-3}$. However, disentangling this effect from the genuine behavior of $\chi_{\text{nem}}^{\text{As}}$ under strong applied strain is highly nontrivial. An interesting corollary to the above discussion is the interpretation of temperature-dependent measurements under constant uniaxial stress as reported in several neutron scattering and optical spectroscopy studies in various Fe SC materials [14,15,29,49–51]. Because of the strong softening of the Young's modulus along the orthorhombic axis close to T_S , the strain associated to the

stress applied to the sample is strongly enhanced near T_S and even diverges at T_S . This leads to much larger temperature-dependent nonlinear effects than by working under constant nominal strain, and makes the interpretation of constant stress measurements in terms of nematic susceptibilities problematic.

Finally, we discuss the origin of the strain-induced activation of the As phonon in $x'y'$ geometry. Up to now, we have assigned it to a finite nematic order parameter from symmetry-based arguments. However, the activation has in general been assigned to the emergence of the stripelike SDW order at $T_N \approx T_S$, with only a minor role for the nematic order itself [30,43,44]. In Ref. [30], it was argued that, only with the inclusion of magnetism can density functional theory calculations reproduce the experimental Raman features of the As phonon in the xx and yy polarization configurations. Also, the magnetic origin is suggested by the comparison between Raman spectra obtained on BaFe_2As_2 , Co-doped BaFe_2As_2 with split T_S and T_N , and FeSe, which displays a structural but no magnetic transition [43]. In principle, this question can be experimentally addressed in samples with sufficiently split T_S and T_N transitions but, unfortunately, the As phonon intensity is, in general, too small in such samples to convincingly settle this issue. Here we address it by noting that the temperature dependence of the As phonon intensity under constant anisotropic stress is expected to be rather different between the magnetic and nematic scenario. Indeed, the nematic transition is no longer well-defined and instead becomes a crossover under B_{2g} stress, akin to a ferromagnet under an applied magnetic field. The SDW transition, however, remains sharply defined since strain does not couple linearly to the magnetic order parameter [52].

The temperature dependence of $|\phi_{\text{nem}}^{\text{As}}|$ at constant strain and the corresponding spectra are displayed in Fig. 5. Due to the crystal break before these temperature-dependent measurements, there is some uncertainty in the determination of the neutral point corresponding to $\epsilon_{xx}^{\text{nom}} = 0$. Based on strain-dependent spectra at fixed temperatures (Fig. 3), we estimate the low-strain measurements to be under small compressive strains, in absolute value smaller than 2×10^{-3} . As for the strain-dependent measurements, the phonon was fitted using a Fano line shape to extract its intensity (see Appendix A). For small strains, the phonon intensity has a relatively sharp onset close to the strain-free $T_{S,N} = 138$ K, with a small tail above 140 K. Except for the small tail above 138 K, this agrees with previous Raman measurements under nominally zero strain [53,54]. At high compressive strain, $\epsilon_{xx}^{\text{nom}} \sim -6.4 \times 10^{-3}$, the sharp onset is replaced by a very broad tail extending well above the strain-free $T_{S,N}$. We note that nuclear magnetic resonance (NMR) studies of Ba122 under uniaxial strain show a relatively weak effect of strain on T_N , with a shift of at most 10 K for $\epsilon_{xx}^{\text{nom}} \sim -6 \times 10^{-3}$ [17]. Within our experimental accuracy, no additional jump or anomaly which could be assigned to T_N is detected in the temperature dependence of $|\phi_{\text{nem}}^{\text{As}}|$. This indicates a minimal impact of the SDW order on the phonon intensity. Note, however, that the effective phonon energy extracted from the Fano analysis bears fingerprints of T_N , as can be inferred from the change in phonon line shape observed around 140 K (see Appendix A).

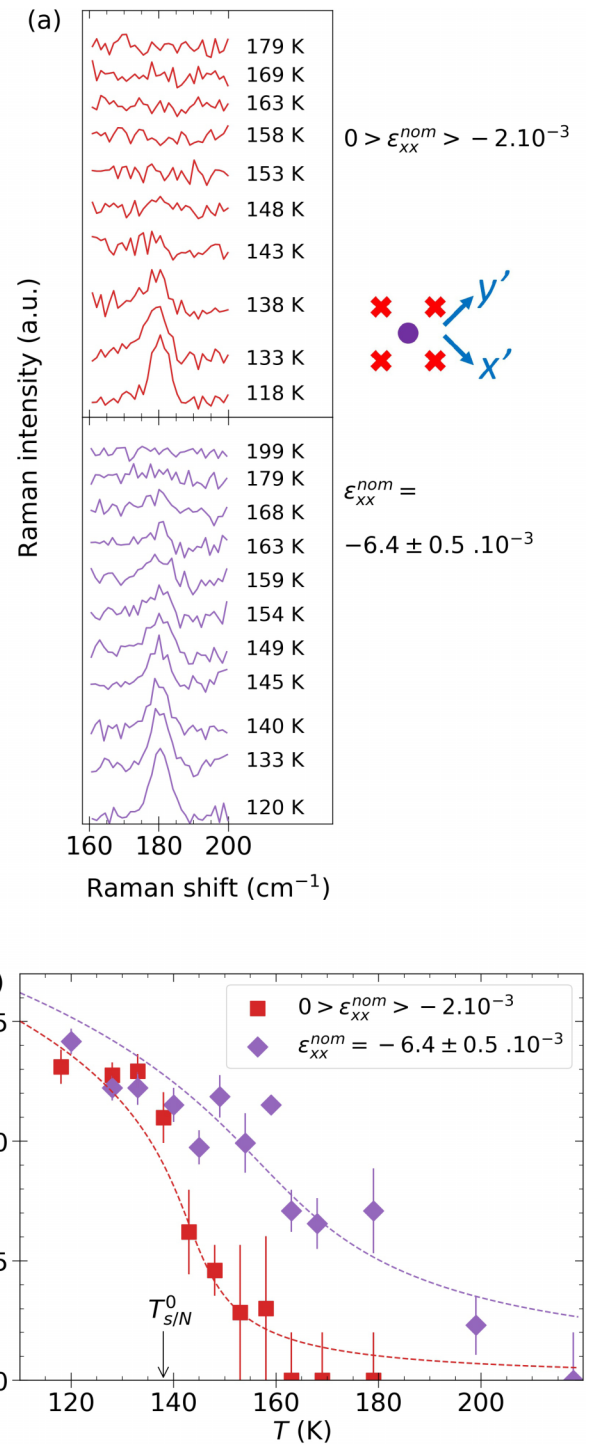


FIG. 5. (a) Evolution of the As phonon Raman spectra in the $x'y'$ polarization configuration crossing T_S at fixed strains. The evaluation of the strain for the small strain series (in red) is complicated by the fact that the sample was broken at that time. We estimated the strain value to be close to 0, with a maximum error evaluated by comparing the spectrum at 143 K with the series at 145 K displayed in Fig. 3. (b) Dependence of As phonon nematic order parameter $|\phi_{\text{nem}}^{\text{As}}|$ with temperature at fixed strains. The dashed lines are guides to the eye following a Landau-type behavior of the order parameter with a symmetry-breaking field five times larger for the purple line compared to the red line (see Appendix D).

Overall, the qualitative behavior of $|\phi_{\text{nem}}^{\text{As}}|$ is consistent with the temperature dependence of an Ising order parameter under a symmetry-breaking field, where the sharp phase transition at zero field is replaced by a smooth crossover at high field [see lines in Fig. 5(b) and Appendix D]. It should be noted that stress, not strain, is the conjugate field of the orthorhombic distortion. Therefore, if the applied B_{2g} strain is smaller than the spontaneous structural distortion, we expect a first-order phase transition to a twinned-domain sample, at a temperature where the spontaneous structural distortion matches the applied strain, i.e., below the strain-free T_S [13]. For our large strain data (purple points), the applied strain exceeds this spontaneous structural distortion, and the first-order transition does not occur. It could, however, be present in our low strain data (red points), close to T_S^0 , but it cannot be clearly resolved within our experimental accuracy. Importantly, the observed evolution from a relatively sharp onset to a very broad crossover of $|\phi_{\text{nem}}^{\text{As}}|$ versus temperature cannot be understood if the activation of the As phonon is driven by a magnetic origin. In a magnetic scenario, we would expect a sharp onset at the still well-defined T_N , in sharp contrast with the broad crossover observed under strong applied strain.

A potential complication in quantitatively analyzing the data is the fact that despite working at constant $\epsilon_{xx}^{\text{nom}}$, the B_{2g} strain could be temperature dependent due to the softening of the lattice. This effect is certainly present at moderate strains. However, as we argue in Appendix C, we expect the lattice to stiffen considerably at these high strain levels. In that case, the shear modulus temperature dependence becomes much weaker [20,48] and likely plays a marginal role in the observed temperature dependence for strain above 5×10^{-3} . We therefore conclude that in Ba122 the anisotropy of the Raman tensor elements as measured via $|\phi_{\text{nem}}^{\text{As}}|$ reflects nematic rather than magnetic degrees of freedom. As such, this quantity appears to be a faithful probe of the electronic nematic order parameter.

In conclusion, using a low-temperature polarization-resolved elasto-Raman setup, we have shown that the As phonon can provide a valuable local probe of nematic domains and order parameter in the model system Ba122. This has allowed us to track the nematic order parameter both as a function of strain and temperature above and below the nematic transition temperature. We have also stressed some possible pitfalls that must be taken into account when interpreting uniaxial strain data near a structural instability. Our paper illustrates the interest of combining a symmetry-resolved stimulus like uniaxial strain with a symmetry-resolved probe like Raman. While the As phonon remains a rather indirect way to probe electronic nematic degrees of freedom in a metallic system with respect to elastoresistivity and electronic Raman scattering for, e.g., our data demonstrate that elasto-Raman studies of optical phonon could be a valuable tool to study nematic degrees of freedom in insulators where the aforementioned techniques are not accessible.

ACKNOWLEDGMENTS

The authors thank Indranil Paul for helpful discussions and a careful reading of the paper. Funding from Agence

Nationale de la Recherche grant IFAS (Grant No. ANR-18-CE92-0020-02) is acknowledged.

APPENDIX A: FANO LINE-SHAPE FITTING

Close to T_S , the Raman As phonon displays a significant asymmetry which is linked to its coupling to electronic degrees of freedom. The coupling makes the extraction of the phonon intensity nontrivial, requiring a fit to disentangle the phononic and electronic contributions. The coupling between a discrete mode, here the As phonon, and a broad continuum, here the electronic excitations, leads to a characteristic asymmetrical line shape which can be described by a coupled mode analysis as depicted in the Fano model. Following Klein's approach [55], we consider a bare phonon mode, expressed by a Dirac δ function with area πt_{ph} coupled to a featureless electronic continuum ρ which couples to light with an amplitude t_e . The imaginary part of the coupled electron-phonon response χ , the quantity that is measured in a Raman scattering experiment, takes the form

$$\chi''(\omega) = \frac{t_e^2 \pi \rho (\omega_0 - \omega - v t_{\text{ph}}/t_e)^2}{(\omega_0 - \omega)^2 + (v^2 \pi \rho)^2}, \quad (\text{A1})$$

where v is the electron-phonon coupling parameter and ω_0 is a renormalized effective phonon energy [55]. For the As phonon fitting, we used the following parametrization: $A = \pi \rho t_e^2$, ω_0 , t_{ph} , and $B = \frac{v}{t_e}$. This parametrization has the advantage of explicitly involving the quantity of interest, the bare phonon amplitude t_{ph} , in the minimization routine, thus reducing the standard error on its evaluation. The response then takes the form

$$\chi''(\omega) = A \frac{(\omega_0 - \omega - t_{\text{ph}} B)^2}{(\omega_0 - \omega)^2 + (A B^2)^2}. \quad (\text{A2})$$

This expression was used to fit the As phonon as a function of both strain and temperature to extract the integrated area of the bare phonon mode given by πt_{ph}^2 . To fit the data, it was necessary to add an additional noninteracting background y_0 . For spectra with a well-defined and intense peak, such as at low temperature below T_S and/or large strain, good convergence was found when keeping all parameters free. However, for spectra displaying a weaker peak, we found it necessary to keep constant at least one of the parameters to ensure a more systematic fit convergence and we chose to keep $B = \frac{v}{t_e}$ constant. We checked that the fitted values of ω_0 and t_{ph} were only weakly dependent on different choices of B , typically within the standard error bars of the fits. The fits as a function of strain and temperature are shown in Figs. 6 and 7. The extracted amplitude t_{ph} was used for Figs. 4 and 5 of the main text.

In the temperature dependence under strong strain (Fig. 7), the fits also reveal a small anomaly of ω_0 (about 1 cm^{-1}) at around 145 K (Fig. 8). A similar softening was observed previously at zero strain at $T_{S,N}$ [56]. We believe the observed softening in the high-strain data is due to the SDW transition T_N which remains well-defined even in the presence of strain and is only weakly affected by it, in agreement with NMR data of Kissikov *et al.* [17].

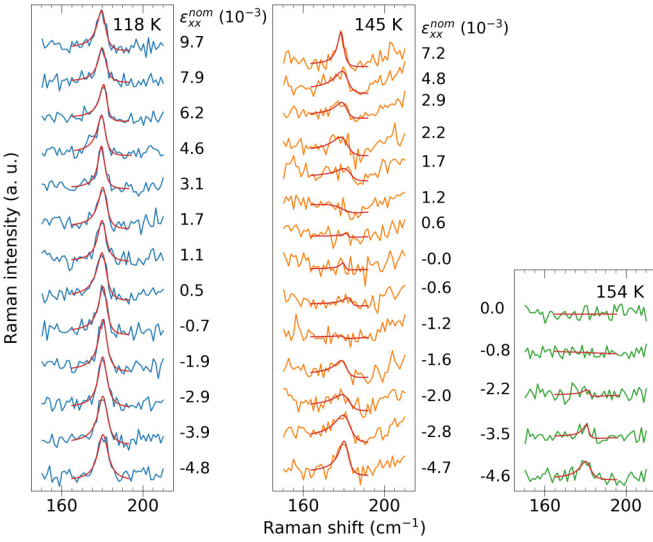


FIG. 6. Fano line-shape fitting of the As phonon as a function of applied strain and at three different temperatures.

APPENDIX B: FINITE-ELEMENT SIMULATION

In this paper, we plotted the different quantities depending on the nominal strain in the x direction $\epsilon_{xx}^{\text{nom}} = \frac{\delta L}{L_0}$, with L_0 the length of the suspended part of the sample when no stress is applied and δL the change of this length upon applied stress. $\epsilon_{xx}^{\text{nom}}$ is different from the nematic strain $\epsilon_{B_{2g}}$, with $\epsilon_{B_{2g}} = \frac{1}{2}(1 + \nu)\mu\epsilon_{xx}^{\text{nom}}$. ν is the Poisson ratio in the ab plane and μ is the strain transmission coefficient through the epoxy glue. In BaFe_2As_2 , the elastic coefficient corresponding to

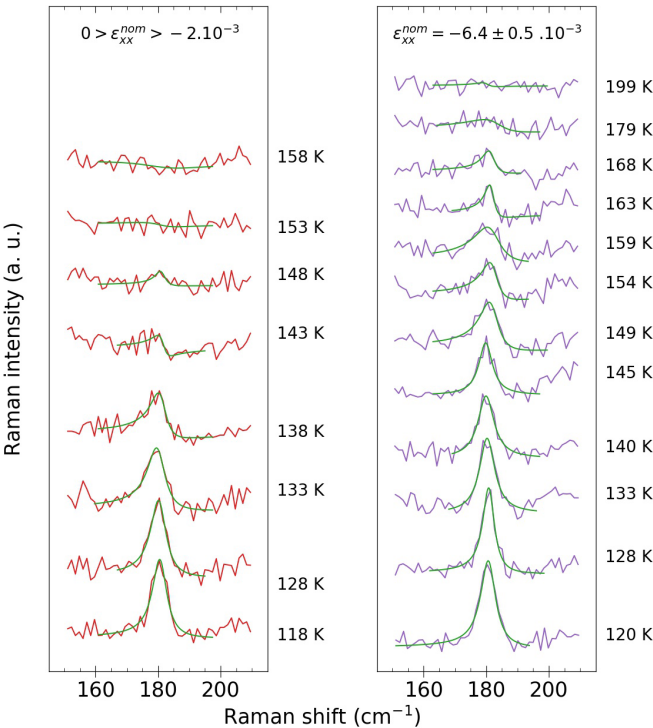


FIG. 7. Fano line-shape fitting of the As phonon as a function of temperature at two different applied strains.

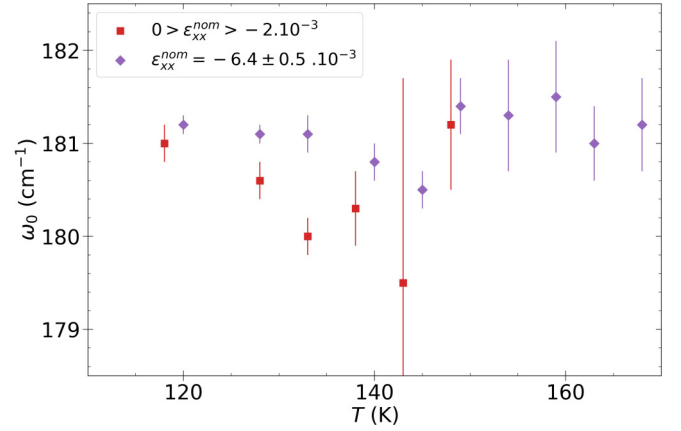


FIG. 8. Temperature dependence of the effective phonon energy ω_0 as extracted from the Fano line-shape fitting. At low strain, the fitting above 148 K yielded very high error bars for ω_0 due to the very weak phonon intensity and the corresponding values are not shown.

B_{2g} strain, C_{66} , strongly softens upon cooling from 300 K to $T_{S/N} \approx 138$ K [46], which results in a strong decrease of the Young modulus in the x direction [57] and an increase of both μ and ν . Therefore, comparing the dependence of $\phi_{\text{nem}}^{\text{As}}$ on $\epsilon_{xx}^{\text{nom}}$ at different temperatures to evaluate the susceptibility can be misleading. To tackle this issue, we conducted finite element simulations to evaluate ϵ_{xx} and $\epsilon_{B_{2g}} = \epsilon_{x'y'}$.

Figure 9(a) shows the geometry of the model built for the simulation. We took 15 GPa and 0.3, respectively, for the Young modulus and Poisson ratio of the Stycast 2850FT epoxy glue [58] and 105 GPa and 0.33 for the titanium plates [37]. On first approximation, we considered these quantities to remain constant between 300 K and $T_{S/N}$, which probably leads to a slight overestimation of ϵ_{xx} and $\epsilon_{B_{2g}}$ at 300 K, as the epoxy glue is softer at high temperature. For BaFe_2As_2 , we used the complete elastic tensor with the elasticity coefficients in the $x'y'z$ frame taken from Ref. [59]. We extrapolated to 300 K the few elasticity coefficients not measured at room temperature by Ref. [59]. In particular, we took for C_{66} 8, 15, 26, and 35 GPa, respectively, for 145, 154, 188, and 300 K. We chose 20 μm as the upper limit for the size of the finite elements in the sample domain, and some larger sizes in the epoxy glue and titanium domains.

The results for the simulation at the four temperatures for both ϵ_{xx} and $\epsilon_{B_{2g}}$ are plotted in Fig. 9(b). We observe that the strain is homogeneous in the middle region of the sample, where the laser spot is located, on a scale much larger than the spot size of $\sim 50 \mu\text{m}$. Figure 9(b) shows results for the strain along an x line in the bulk of the sample, but we checked that the strain displays a perfect homogeneity along the z direction, and a sufficiently good one in the y direction on the scale of the spot size.

Because of the strong inhomogeneity of ϵ_{xx} along the length outside the middle region, with regions for $|x| > 500 \mu\text{m}$ being quite low strained, the resulting ϵ_{xx} in the middle region can exceed the applied strain $\epsilon_{xx}^{\text{nom}}$. This excess is weak at 145 K (3%) but strongly increases as we take $C_{66} \rightarrow 0$ GPa: the simulations give $\mu = 1.6/2.2/4.3$ for $C_{66} = 1$ GPa/100 MPa/0 GPa, with a simultaneous drastic

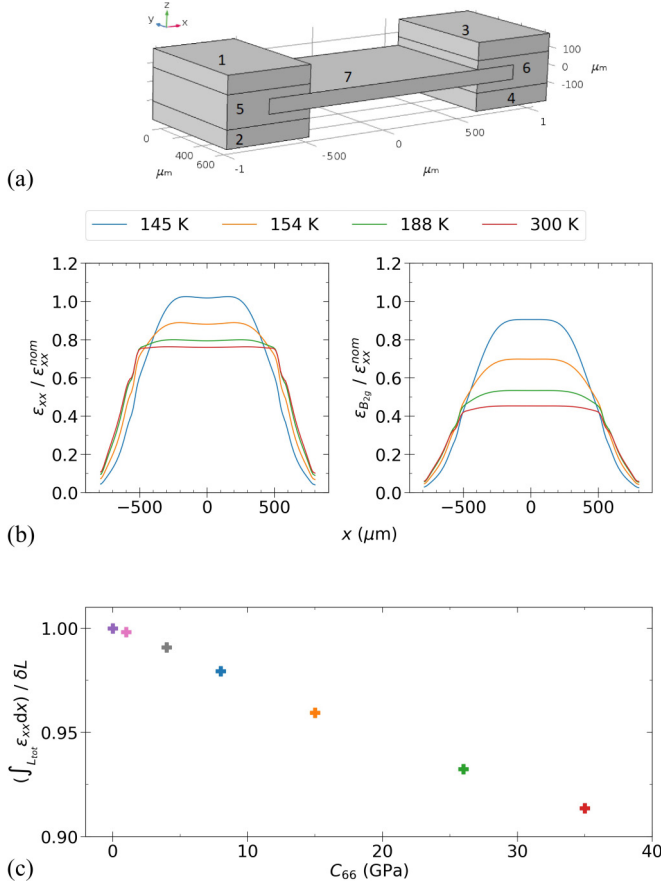


FIG. 9. (a) Geometry of the built model. The domains correspond to: 1 to 4 : titanium plates; 5 and 6 : epoxy glue; 7 : sample. A displacement is given to domains 1 and 2, whereas domains 3 and 4 are held still. (b) Contribution of ϵ_{xx} and $\epsilon_{B_{2g}}$ in the total strain $\epsilon_{xx}^{\text{nom}}$. (c) Comparison between the maximum displacement in the sample and the applied displacement.

reduction of the size of the middle region of homogeneity. This inhomogeneity enhancement might be problematic when probing the sample very close to T_S but we note that in a real sample local defects will likely play an important role not captured by our simulation.

In Fig. 9(c), we check that, for a given displacement δL , the maximum displacement in the sample, i.e., the displacement at the mobile extremity $u = \int_{L_{\text{tot}}} \epsilon_{xx} dx$, with L_{tot} the total length of the sample (1600 μm), is lower than $\delta L = \int_{L_{\text{tot}}} \epsilon_{xx}^{\text{nom}} dx$, even for $C_{66} \rightarrow 0$ GPa. This ratio can serve as a proxy to estimate the amount of strain in the epoxy glue.

In the following, we consider only the values of ϵ_{xx} and $\epsilon_{B_{2g}}$ in the middle region [at $x = 0$ μm in Fig. 9(b)]. As expected, both quantities increase with decreasing T . In particular, $\frac{\epsilon_{B_{2g}}(145 \text{ K})}{\epsilon_{B_{2g}}(154 \text{ K})} \approx 1.3$. This significant ratio likely participates in the $\frac{\partial \phi_{\text{nem}}^{\text{As}}}{\partial \epsilon_{xx}^{\text{nom}}}$ difference between the two temperatures evidenced in Fig. 4, but is not enough to explain it. Our simulations confirm that the change of slope is not merely an effect of the change of transmission, but $\chi_{\text{nem}}^{\text{As}}$ is quantitatively modified when approaching $T_{S/N}$ from above, thus supporting the view that it at least partly reflects the underlying electronic nematic susceptibility.

APPENDIX C: SHEAR MODULUS UNDER FINITE STRESS

At vanishingly small stress, the shear modulus softens to essentially zero at T_S as observed in ultrasound and Young's modulus measurements [46,57,60]. This softening can complicate the interpretation of temperature-dependent data under constant nominal strain $\epsilon_{xx}^{\text{nom}}$ reported in Fig. 5 since its B_{2g} component will depend significantly on temperature close to T_S even if the nominal strain $\epsilon_{xx}^{\text{nom}}$ is kept constant [20]. Published elastic measurements of C_{66} can be used to evaluate both the Poisson ratio ν and the transmission coefficient and thus deduce the B_{2g} component of the applied strain in the low strain limit. This is discussed in the main text and in Appendix B. Outside this regime, however, we cannot rely on elastic measurement data. In particular, under strong stress the lattice is expected to stiffen due to the finite nematic order parameter, thus suppressing the observed softening and resulting in less temperature-dependent Poisson ratio and transmission coefficient. Here we discuss this effect and its potential impact on the temperature-dependent data under high strain shown in Fig. 5. For this, we need to include explicitly both electronic and lattice degrees of freedom in the Landau free energy. The Landau free energy of a coupled nematic-orthorhombic transition includes an electron nematic order parameter ϕ and a lattice distortion ϵ both belonging to the B_{2g} representation of D_{4h} point group. They are coupled bilinearly via a nematoelastic constant $\lambda > 0$. We assume that the system is under a stress $\sigma > 0$ whose B_{2g} component is coupled linearly to ϵ . Here we will limit ourselves to ϕ^4 terms in the expansion:

$$F = \frac{r}{2} \phi^2 + \frac{u}{4} \phi^4 + \frac{C_{66}^0}{2} \epsilon^2 - \lambda \phi \epsilon - \sigma \epsilon. \quad (\text{C1})$$

C_{66}^0 is the bare shear modulus which we will assume to be temperature independent and r is the inverse of the nematic susceptibility which follows a mean-field like behavior $r = a(T - T_0)$. T_0 is the bare nematic phase transition in the absence of a coupling to the lattice. σ and ϵ are the B_{2g} components of the stress and strain tensors, respectively.

We first minimize the free energy with respect to ϕ and ϵ , giving

$$\sigma = C_{66}^0 \epsilon - \lambda \phi, \quad (\text{C2})$$

$$\epsilon = \frac{r \phi + u \phi^3}{\lambda}. \quad (\text{C3})$$

The two equations can be combined to give an equation for the nematic order parameter under constant stress:

$$\left(r - \frac{\lambda^2}{C_{66}^0} \right) \phi + u \phi^3 - \frac{\lambda \sigma}{C_{66}^0} = 0. \quad (\text{C4})$$

Note that the nematic transition has been shifted to higher temperature T_S due to the finite nematoelastic coupling: $T_S = T_0 + \frac{\lambda^2}{a C_{66}^0}$. The renormalized shear modulus C_{66} due to nematoelastic coupling can be computed using the partial derivatives of ϕ :

$$C_{66} = \frac{\partial \phi}{\partial \epsilon} \frac{\partial \sigma}{\partial \phi}. \quad (\text{C5})$$

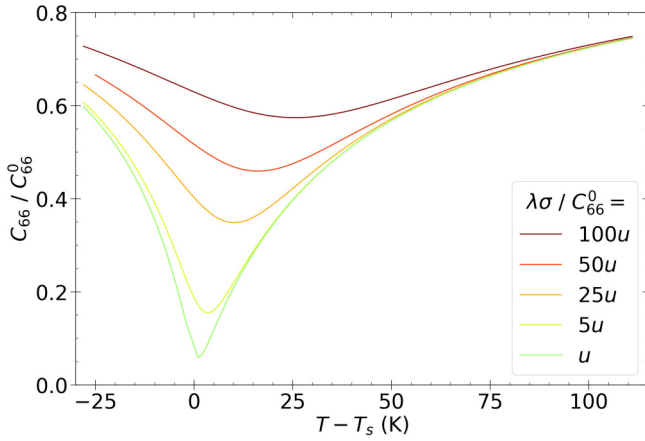


FIG. 10. Temperature dependence of the shear modulus C_{66} under increasing B_{2g} stress σ . Here we have used $T_S = 138$ K, $T_0 = 100$ K, $u = 1$, $a = 1$, and $C_{66}^0 = 30$ GPa.

Using the minimization conditions the partial derivatives are given by:

$$\frac{\partial \epsilon}{\partial \phi} = \frac{1}{\lambda} (r + 3u\phi^2), \quad (\text{C6})$$

$$\frac{\partial \sigma}{\partial \phi} = C_{66}^0 \frac{\partial \epsilon}{\partial \phi} - \lambda. \quad (\text{C7})$$

Inserting into the expression of C_{66} , we get

$$C_{66} = C_{66}^0 - \lambda \frac{\partial \phi}{\partial \epsilon} = C_{66}^0 - \frac{\lambda^2}{r + 3u\phi^2}. \quad (\text{C8})$$

Using Eq. (C8) and the temperature dependence of the nematic order parameter under constant stress σ Eq. (C4), we can plot the temperature dependence of the shear modulus under finite stress (Fig. 10).

For sufficiently strong stress, the softening of the shear modulus C_{66} is indeed strongly suppressed, and we expect the Poisson and transmission ratio to be much less temperature dependent. The question is then to evaluate to which regime the temperature-dependent measurements under high-strain of Fig. 5 correspond to. According to x-ray data under strain of Sanchez *et al.* [20] on a Ba122 crystal with 3% Co doping, both the Poisson ratio and the transmission coefficient become essentially temperature independent for nominal applied strains $\epsilon_{xx}^{\text{nom}} > 5 \cdot 10^{-3}$. Since the measurements of Fig. 5 were performed at $|\epsilon_{xx}^{\text{nom}}| > 5 \cdot 10^{-3}$, we are likely in the regime where the shear modulus is essentially temperature independent.

From our temperature-dependent Raman data under strong strain, we can also estimate in which regime we are. Indeed, assuming the As phonon intensity in the B_{2g} representation is a good proxy of the square of the nematic order parameter ϕ^2 , we see that the nematic order parameter under strong strain (above $|\epsilon_{xx}^{\text{nom}}| = 4 \cdot 10^{-3}$) at 145 K is very close (within 25%) to the saturated value at 118 K (Figs. 4 and 5). Using this information, we can infer the amount of shear modulus softening near T_S (where it is strongest) using the expression of the shear modulus as a function of the nematic order parameter ϕ . If we assume that the nematic order parameter under stress at $T_S = 138$ K is a fraction $\alpha^{1/2}$ of the low-temperature

(saturated) nematic order parameter at zero stress:

$$\phi^2(T_S, \sigma \neq 0) = \alpha \phi^2(T = 0 \text{ K}, \sigma = 0) = \frac{\alpha a T_S}{u}. \quad (\text{C9})$$

Substituting into the equation for the shear modulus Eq. (C8), we can estimate its value at T_S :

$$C_{66}(T_S) = C_{66}^0 - \frac{\lambda^2}{a(T_S - T_0) + 3aT_S\alpha}. \quad (\text{C10})$$

Using $\frac{\lambda^2}{a} = C_{66}^0(T_S - T_0)$, we obtain

$$C_{66}(T_S) = C_{66}^0 \left(1 - \frac{T_S - T_0}{(1 + 3\alpha)T_S - T_0} \right). \quad (\text{C11})$$

For Ba122, we have $T_S = 138$ K and from shear modulus and Raman data (under zero strain) $T_0 = 100$ K [25,46]. Taking a conservative $\alpha = 0.5$ (70% of the low-temperature order parameter at $T = 145$ K $\sim T_S$ at high strain), we obtain $C_{66} \sim 0.84C_{66}^0$. This indicates that the complete softening of C_{66} at zero strain is replaced by a much smaller softening of about 16% at high strain giving an upper bound on the temperature evolution of C_{66} . In turn a 16% change in C_{66} will imply a change in the Poisson ratio $1 + \nu$. To evaluate this, we use the relationship between the C_{66} and $1 + \nu$: $1 + \nu = \frac{2C}{C + C_{66}}$, with $C = \frac{1}{2}(C_{11} + C_{12}) - \frac{C_{13}^2}{C_{33}}$. Except C_{66} , the elastic coefficients are weakly temperature dependent. Using $C_{11} = 95$ GPa, $C_{12} = C_{13} = 17$ GPa, $C_{33} = 75$ GPa, and $C_{66} = 35$ GPa [59], we obtain a change of 7% in $1 + \nu$ between T_S and high temperatures. From the simulations (Appendix B), the change in the transmission ratio μ will be even less. To conclude, changes in the B_{2g} component of the strain as a function of temperature are unlikely to significantly affect the observed temperature dependence of $\phi_{\text{nem}}^{\text{As}}$ under high strain reported in Fig. 5.

APPENDIX D: NEMATIC ORDER PARAMETER UNDER A SYMMETRY-BREAKING FIELD

The behavior of the nematic order parameter under a symmetry breaking field can be captured by a Landau free energy

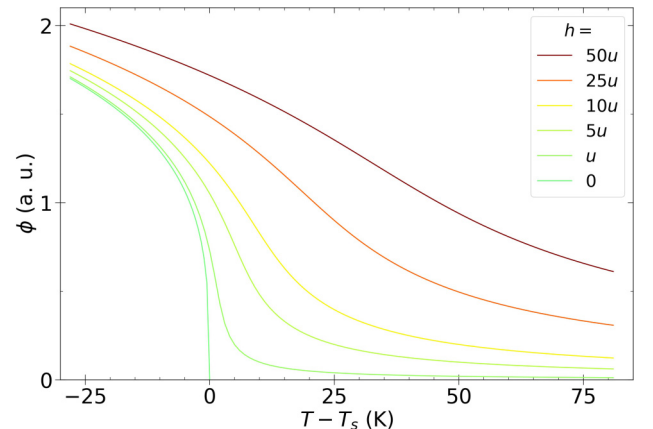


FIG. 11. Temperature dependence of the nematic order parameter ϕ under increasing symmetry-breaking field h . Parameters used are $(a, u, w) = (1, 1, 3)$.

with an electron nematic order parameter ϕ and a symmetry-breaking field h :

$$F = \frac{r}{2}\phi^2 + \frac{u}{4}\phi^4 + \frac{w}{6}\phi^6 - h\phi. \quad (\text{D1})$$

In our case, h is a B_{2g} field which couples linearly to ϕ and $r = a(T - T_S)$ (T_S is the renormalized nematic transition temperature). Minimizing the free energy with respect to ϕ ,

we obtain

$$r\phi + u\phi^3 + w\phi^5 - h = 0. \quad (\text{D2})$$

The above equation was solved for ϕ numerically as a function of temperature T and for various field h keeping all other parameters constant (Figs. 5 and 11). In Fig. 5, the parameters used were $h = 5u$ and $h = 25u$ for the low and high strain data, respectively.

-
- [1] J.-H. Chu, H.-H. Kuo, J. G. Analytis, and I. R. Fisher, *Science* **337**, 710 (2012).
- [2] C. W. Hicks, D. O. Brodsky, E. A. Yelland, A. S. Gibbs, J. A. N. Bruin, M. E. Barber, S. D. Edkins, K. Nishimura, S. Yonezawa, Y. Maeno *et al.*, *Science* **344**, 283 (2014).
- [3] A. Steppke, L. Zhao, M. E. Barber, T. Scaffidi, F. Jerzembeck, H. Rosner, A. S. Gibbs, Y. Maeno, S. H. Simon, A. P. Mackenzie *et al.*, *Science* **355**, eaaf9398 (2017).
- [4] H.-H. Kim, S. M. Souliou, M. E. Barber, E. Lefrançois, M. Minola, M. Tortora, R. Heid, N. Nandi, R. A. Borzi, G. Garbarino *et al.*, *Science* **362**, 1040 (2018).
- [5] R. M. Fernandes, A. V. Chubukov, and J. Schmalian, *Nat. Phys.* **10**, 97 (2014).
- [6] S. Hosoi, K. Matsuura, K. Ishida, H. Wang, Y. Mizukami, T. Watashige, S. Kasahara, Y. Matsuda, and T. Shibauchi, *Proc. Natl. Acad. Sci.* **113**, 8139 (2016).
- [7] H.-H. Kuo, J.-H. Chu, J. C. Palmstrom, S. A. Kivelson, and I. R. Fisher, *Science* **352**, 958 (2016).
- [8] P. Malinowski, Q. Jiang, J. J. Sanchez, J. Mutch, Z. Liu, P. Went, J. Liu, P. J. Ryan, J.-W. Kim, and J.-H. Chu, *Nat. Phys.* **16**, 1189 (2020).
- [9] A. V. Maharaj, E. W. Rosenberg, A. T. Hristov, E. Berg, R. M. Fernandes, I. R. Fisher, and S. A. Kivelson, *Proc. Natl. Acad. Sci.* **114**, 13430 (2017).
- [10] T. Worasaran, M. S. Ikeda, J. C. Palmstrom, J. A. W. Straquadine, S. A. Kivelson, and I. R. Fisher, *Science* **372**, 973 (2021).
- [11] H.-H. Kuo, M. C. Shapiro, S. C. Riggs, and I. R. Fisher, *Phys. Rev. B* **88**, 085113 (2013).
- [12] C. W. Hicks, M. E. Barber, S. D. Edkins, D. O. Brodsky, and A. P. Mackenzie, *Rev. Sci. Instrum.* **85**, 065003 (2014).
- [13] J. M. Bartlett, A. Steppke, S. Hosoi, H. Noad, J. Park, C. Timm, T. Shibauchi, A. P. Mackenzie, and C. W. Hicks, *Phys. Rev. X* **11**, 021038 (2021).
- [14] C. Mirri, A. Dusza, S. Bastelberger, M. Chinotti, L. Degiorgi, J.-H. Chu, H.-H. Kuo, and I. R. Fisher, *Phys. Rev. Lett.* **115**, 107001 (2015).
- [15] C. Mirri, A. Dusza, S. Bastelberger, M. Chinotti, J.-H. Chu, H.-H. Kuo, I. R. Fisher, and L. Degiorgi, *Phys. Rev. B* **93**, 085114 (2016).
- [16] T. Kissikov, R. Sarkar, B. T. Bush, M. Lawson, P. C. Canfield, and N. J. Curro, *Rev. Sci. Instrum.* **88**, 103902 (2017).
- [17] T. Kissikov, R. Sarkar, M. Lawson, B. T. Bush, E. I. Timmons, M. A. Tanatar, R. Prozorov, S. L. Bud'ko, P. C. Canfield, R. M. Fernandes *et al.*, *Nat. Commun.* **9**, 1058 (2018).
- [18] E. F. Andrade, A. N. Berger, E. P. Rosenthal, X. Wang, L. Xing, X. Wang, C. Jin, R. M. Fernandes, A. J. Millis, and A. N. Pasupathy, [arXiv:1812.05287](https://arxiv.org/abs/1812.05287).
- [19] H. Pfau, S. D. Chen, M. Yi, M. Hashimoto, C. R. Rotundu, J. C. Palmstrom, T. Chen, P. C. Dai, J. Straquadine, A. Hristov, R. J. Birgeneau, I. R. Fisher, D. Lu, and Z. X. Shen, *Phys. Rev. Lett.* **123**, 066402 (2019).
- [20] J. J. Sanchez, P. Malinowski, J. Mutch, J. Liu, J.-W. Kim, P. J. Ryan, and J.-H. Chu, *Nat. Mater.* **20**, 1519 (2021).
- [21] A. T. Hristov, M. S. Ikeda, J. C. Palmstrom, P. Walmsley, and I. R. Fisher, *Phys. Rev. B* **99**, 100101(R) (2019).
- [22] M. S. Ikeda, T. Worasaran, E. W. Rosenberg, J. C. Palmstrom, S. A. Kivelson, and I. R. Fisher, *Proc. Natl. Acad. Sci.* **118**, e2105911118 (2021).
- [23] F. Caglieris, C. Wuttke, X. C. Hong, S. Sykora, R. Kappenberger, S. Aswartham, S. Wurmehl, B. Büchner, and C. Hess, *npj Quantum Mater.* **6**, 27 (2021).
- [24] Y. Gallais, R. M. Fernandes, I. Paul, L. Chauvière, Y.-X. Yang, M.-A. Méasson, M. Cazayous, A. Sacuto, D. Colson, and A. Forget, *Phys. Rev. Lett.* **111**, 267001 (2013).
- [25] Y. Gallais and I. Paul, *C. R. Phys.* **17**, 113 (2016).
- [26] V. K. Thorsmølle, M. Khodas, Z. P. Yin, C. Zhang, S. V. Carr, P. Dai, and G. Blumberg, *Phys. Rev. B* **93**, 054515 (2016).
- [27] F. Kretzschmar, T. Böhm, U. Karahasanović, B. Muschler, A. Baum, D. Jost, J. Schmalian, S. Caprara, M. Grilli, C. Di Castro *et al.*, *Nat. Phys.* **12**, 560 (2016).
- [28] P. Massat, D. Farina, I. Paul, S. Karlsson, P. Strobel, P. Toulemonde, M.-A. Méasson, M. Cazayous, A. Sacuto, S. Kasahara *et al.*, *Proc. Natl. Acad. Sci.* **113**, 9177 (2016).
- [29] X. Ren, L. Duan, Y. Hu, J. Li, R. Zhang, H. Luo, P. Dai, and Y. Li, *Phys. Rev. Lett.* **115**, 197002 (2015).
- [30] A. Baum, Y. Li, M. Tomić, N. Lazarević, D. Jost, F. Löffler, B. Muschler, T. Böhm, J.-H. Chu, I. R. Fisher, R. Valentí, I. I. Mazin, and R. Hackl, *Phys. Rev. B* **98**, 075113 (2018).
- [31] P. A. Fleury and J. M. Worlock, *Phys. Rev.* **174**, 613 (1968).
- [32] E. Anastassakis and E. Burstein, *J. Phys. Chem. Solids* **32**, 563 (1971).
- [33] S. Ganesan, A. A. Maradudin, and J. Oitmaa, *Ann. Phys.* **56**, 556 (1970).
- [34] F. E. A. Melo and F. Cerdeira, *Phys. Rev. B* **26**, 720 (1982).
- [35] P. Merle, J. Pascual, J. Camassel, and H. Mathieu, *Phys. Rev. B* **21**, 1617 (1980).
- [36] E. Anastassakis, A. Pinczuk, E. Burstein, F. H. Pollak, and M. Cardona, *Solid State Commun.* **88**, 1053 (1993).
- [37] M. S. Ikeda, T. Worasaran, J. C. Palmstrom, J. A. W. Straquadine, P. Walmsley, and I. R. Fisher, *Phys. Rev. B* **98**, 245133 (2018).
- [38] L. Chauvière, Y. Gallais, M. Cazayous, M. A. Méasson, A. Sacuto, D. Colson, and A. Forget, *Phys. Rev. B* **84**, 104508 (2011).

- [39] K. Kuroki, H. Usui, S. Onari, R. Arita, and H. Aoki, *Phys. Rev. B* **79**, 224511 (2009).
- [40] T. Yildirim, *Phys. Rev. Lett.* **102**, 037003 (2009).
- [41] F. Yndurain and J. M. Soler, *Phys. Rev. B* **79**, 134506 (2009).
- [42] C.-H. Lee, A. Iyo, H. Eisaki, H. Kito, M. Teresa Fernandez-Diaz, T. Ito, K. Kihou, H. Matsuhata, M. Braden, and K. Yamada, *J. Phys. Soc. Jpn.* **77**, 083704 (2008).
- [43] S.-F. Wu, W.-L. Zhang, V. K. Thorsmølle, G. F. Chen, G. T. Tan, P. C. Dai, Y. G. Shi, C. Q. Jin, T. Shibauchi, S. Kasahara, Y. Matsuda, A. S. Sefat, H. Ding, P. Richard, and G. Blumberg, *Phys. Rev. Research* **2**, 033140 (2020).
- [44] N. A. García-Martínez, B. Valenzuela, S. Ciuchi, E. Cappelluti, M. J. Calderón, and E. Bascones, *Phys. Rev. B* **88**, 165106 (2013).
- [45] M. Rotter, M. Tegel, D. Johrendt, I. Schellenberg, W. Hermes, and R. Pöttgen, *Phys. Rev. B* **78**, 020503(R) (2008).
- [46] M. Yoshizawa, D. Kimura, T. Chiba, A. Ismayil, Y. Nakanishi, K. Kihou, C.-H. Lee, A. Iyo, H. Eisaki, M. Nakajima *et al.*, *J. Phys. Soc. Jpn.* **81**, 024604 (2012).
- [47] M. Yoshizawa and S. Simayi, *Mod. Phys. Lett. B* **26**, 1230011 (2012).
- [48] A. E. Böhmer and C. Meingast, *C. R. Phys.* **17**, 90 (2016).
- [49] C. Dhital, Z. Yamani, W. Tian, J. Zeretsky, A. S. Sefat, Z. Wang, R. J. Birgeneau, and S. D. Wilson, *Phys. Rev. Lett.* **108**, 087001 (2012).
- [50] X. Lu, K.-F. Tseng, T. Keller, W. Zhang, D. Hu, Y. Song, H. Man, J. T. Park, H. Luo, S. Li, A. H. Nevidomskyy, and P. Dai, *Phys. Rev. B* **93**, 134519 (2016).
- [51] D. W. Tam, Y. Song, H. Man, S. C. Cheung, Z. Yin, X. Lu, W. Wang, B. A. Frandsen, L. Liu, Z. Gong, T. U. Ito, Y. Cai, M. N. Wilson, S. Guo, K. Koshiishi, W. Tian, B. Hitti, A. Ivanov, Y. Zhao, J. W. Lynn, G. M. Luke, T. Berlijn, T. A. Maier, Y. J. Uemura, and P. Dai, *Phys. Rev. B* **95**, 060505(R) (2017).
- [52] A. Cano and I. Paul, *Phys. Rev. B* **85**, 155133 (2012).
- [53] L. Chauvière, Y. Gallais, M. Cazayous, A. Sacuto, M. A. Méasson, D. Colson, and A. Forget, *Phys. Rev. B* **80**, 094504 (2009).
- [54] S.-F. Wu, W.-L. Zhang, L. Li, H.-B. Cao, H.-H. Kung, A. S. Sefat, H. Ding, P. Richard, and G. Blumberg, *Phys. Rev. B* **102**, 014501 (2020).
- [55] M. V. Klein, *Electronic Raman Scattering*, Topics in Applied Physics, Vol. 8 (Springer, Berlin, 1983).
- [56] M. Rahlenbeck, G. L. Sun, D. L. Sun, C. T. Lin, B. Keimer, and C. Ulrich, *Phys. Rev. B* **80**, 064509 (2009).
- [57] A. E. Böhmer, P. Burger, F. Hardy, T. Wolf, P. Schweiss, R. Fromknecht, M. Reinecker, W. Schranz, and C. Meingast, *Phys. Rev. Lett.* **112**, 047001 (2014).
- [58] M. E. Barber, Uniaxial stress technique and investigations of correlated electron systems, Ph.D. thesis, University of St Andrews, United Kingdom, 2018.
- [59] C. Fujii, S. Simayi, K. Sakano, C. Sasaki, M. Nakamura, Y. Nakanishi, K. Kihou, M. Nakajima, C.-H. Lee, A. Iyo *et al.*, *J. Phys. Soc. Jpn.* **87**, 074710 (2018).
- [60] R. M. Fernandes, L. H. VanBebber, S. Bhattacharya, P. Chandra, V. Keppens, D. Mandrus, M. A. McGuire, B. C. Sales, A. S. Sefat, and J. Schmalian, *Phys. Rev. Lett.* **105**, 157003 (2010).